LETTER

Unique Chiro-optical Properties of the Weakly-2D (R-/S-MBA)$_2$CuBr$_4$ Hybrid Material

Ranjan Das, Modasser Hossain, Arup Mahata, Diptikanta Swain, Filippo De Angelis, Pralay K. Santra, and D. D. Sarma*
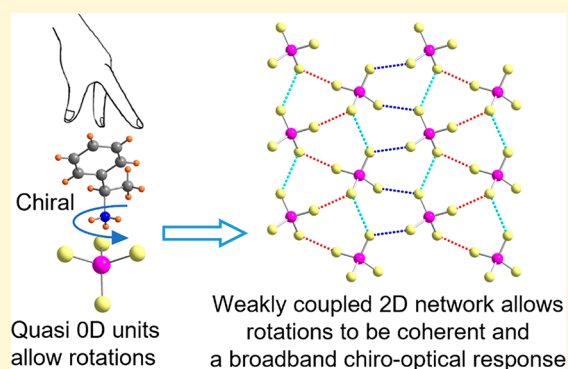
Read Online

ACCESS | Metrics & More | Article Recommendations | Supporting Information

ABSTRACT: We establish that the formally 0D (R-/S-MBA)$_2$CuBr$_4$, containing R-/S-α-methyl benzylamine (R-/S-MBA) connected to highly distorted CuBr$_4$ tetrahedral units in alternating layers, possesses extraordinary chiro-optical properties. The concentration and path length-independent chiral anisotropy factor, g_{CD}, for this compound is the highest in the orange-red part of the visible spectrum reported so far from any hybrid material, arising from a chirality transfer from the organic component to the inorganic layer through the extensive asymmetric hydrogen bonding network and electronic coupling, driving the CuBr$_4$ tetrahedral units to follow the 2$_1$-screw axis. This sensitivity in the orange-red part of the visible spectrum is achieved by incorporating bromine in the copper coordination sphere, which significantly red-shifts the band edge absorption to ∼710 nm compared to ∼490 nm reported for the chloride analogue. DFT/TDDFT calculations allow us to understand the underlying electronic structure responsible for its remarkable optical properties. We find that this compound gets a partial 2D character, crucial for its broadband chiro-optical properties, arising from Cu−Br⋯Br−Cu interactions connecting the otherwise isolated CuBr$_4$ units.

Chiral

Quasi 0D units allow rotations

Weakly coupled 2D network allows rotations to be coherent and a broadband chiro-optical response

Many chiral materials exist in nature, ranging from small amino acids to macromolecular proteins and macroscopic crystals. Due to a lack of inversion symmetry, chiral materials exhibit various interesting physical properties such as circular dichroism (CD),[1] circularly polarized photoluminescence (CPL),[2] nonlinear optical (NLO) effects,[1] ferroelectricity,[3] bulk photovoltaic effects (BPVE),[4] and the ability to rotate the polarization plane of light.[5,6] Chiral organic molecules are abundantly available; however, these generally have very large bandgaps, thereby exhibiting chiro-optical activities in the UV region.[7] In addition, the structural softness of such organic molecules makes it difficult to stack them suitably, and this inability often results in a poor charge transport capability in optoelectronic devices made from such molecules. In this regard, organic−inorganic hybrid (OIH) materials have recently emerged as ideal candidates for optoelectronic devices due to their color tunability through compositions engineering,[8−10] small carrier effective mass,[11] long diffusion length,[12] and high carrier mobility.[13,14] Therefore, it becomes a naturally intriguing issue to seek ways to transfer the abundant chirality of organic molecules to the inorganic units of suitable hybrid materials in order to tailor suitable chiro-optical properties. Accordingly, there exist several reports on lead-based 2D chiral OIH

materials,[2,15−22] but the toxicity of Pb remains a major concern. To overcome this barrier, two Cu-chloride-based chiral and polar 2D OIH materials have been explored so far.[1,3,23] Refs 1 and 23 established giant chiro-optical activities extending until 490 nm, being limited by the bandgap, along with second harmonic generation in (R-/S-MBA)$_2$CuCl$_4$ (MBA$^+$ = α-methyl benzylammonium ion),[1] while ref 3 pointed out a significant magnetoelectrical coupling in (R-/S-MPA)$_2$CuCl$_4$ (MPA$^+$ = β-methyl phenethylammonium ion). The inorganic layers of (R-/S-MPA)$_2$CuCl$_4$ consist of corner sharing CuCl$_6$ octahedra, giving rise to a structurally 2D layer, whereas inorganic layers of the compound (R-/S-MBA)$_2$CuCl$_4$ consist of distorted isolated [CuCl$_4$]$^{2-}$ tetrahedral units defining an essentially 0D structure.

In the present work, we report the Br analogue of this 0D structure, (R-/S-MBA)$_2$CuBr$_4$, which contrastingly forms in a nonpolar space group. This compound has been reported
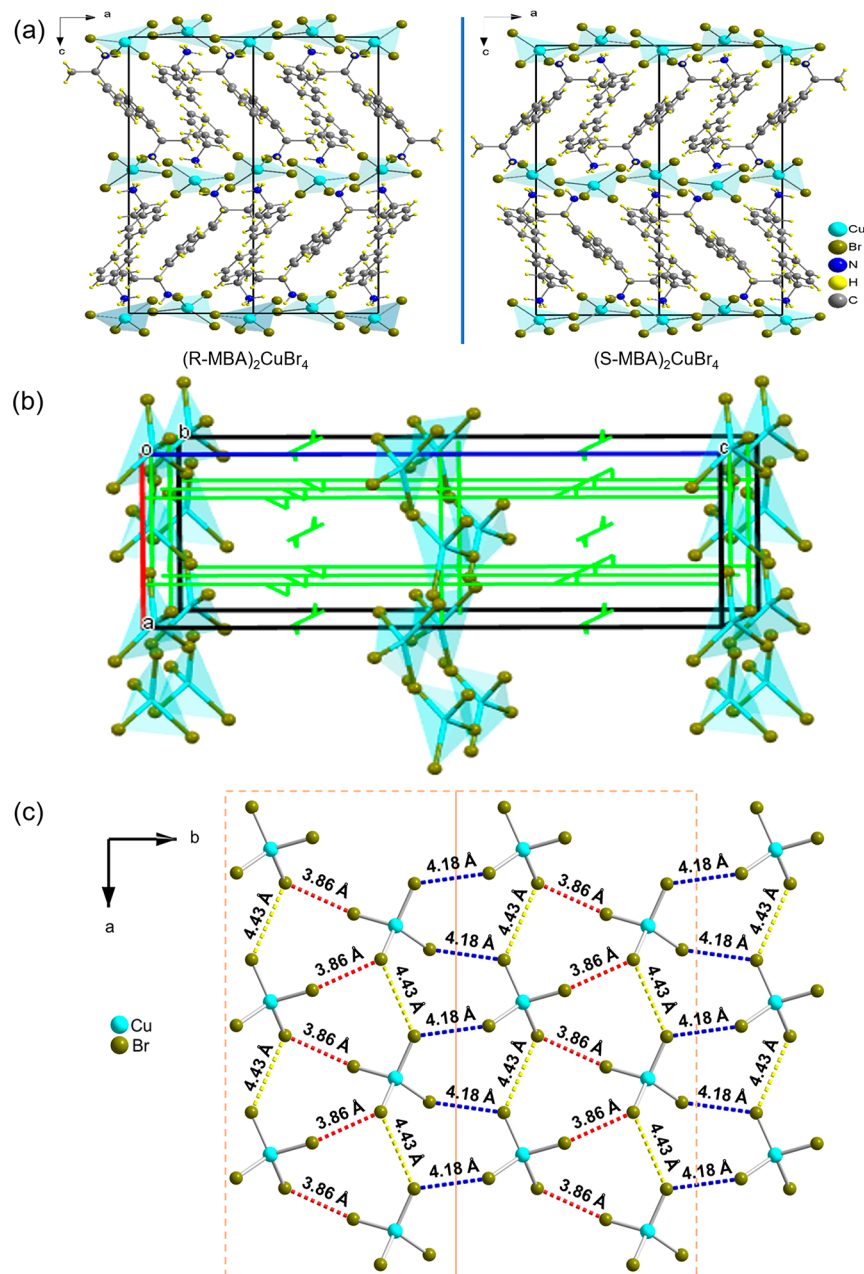
Figure 1. (a) Crystal structure of $(R\text{-}/S\text{-}MBA)_2CuBr_4$ projected along the b-axis (vertical line shows these compounds are mirror images of each other). (b) The tetrahedral $[CuBr_4]^{2-}$ units are connected by 2_1 screw axes, shown by the green line. (c) The 0D $[CuBr_4]^{2-}$ tetrahedral units interact via halide pathways (Cu–Br···Br–Cu), imparting the system with a weak 2D character.

once[24] in the recent literature with the same crystal structure as that determined by us in the present work. Unexpectedly, however, all optical properties, of our sample, such as the absorption edge, and chiro-optical properties, are significantly different, both qualitatively and quantitatively, from those reported in ref 24. While these differences are discussed at a later stage in this article with specific comparisons between the two sets of results, we emphasize here that the properties of our sample are unique and interesting, exhibiting the highest concentration and path length-independent chiral anisotropy factor, g_{CD} (1.1×10^{-2}) in the orange-red part of the visible spectrum among all hybrid halides. This value is comparable to the giant values reported[18,21,23] for only a few other 1D Pb iodide based chiral hybrid materials but at considerably shorter wavelengths (≤ 400 nm). It is approximately one order of

magnitude higher than the maximum g_{CD} ($\sim 10^{-3}$) for similar 2D Pb-based iodide compounds; moreover, in those cases, the chiro-optical properties are limited to wavelengths ≤ 575 nm due to their larger bandgaps. 2D Pb-based bromides also exhibit similarly small ($g_{CD} \sim 10^{-3}\text{–}10^{-4}$) chiral activities while being limited to even shorter wavelengths. Specifically, the Pb-bromide compound, $(MBA)_2PbBr_4$, with the same organic chiral molecule, has a corner-shared 2D layered structure and does not exhibit[17] any chirality, in contrast to the present Cu compound, $(MBA)_2CuBr_4$, with semi-isolated $CuBr_4$ tetrahedral units. Combining detailed theoretical calculations with experimental results, we show that the chirality transfers from the organic component to the quasi-0D $CuBr_4$ tetrahedral units through an extensive asymmetric hydrogen bonding network, inducing these inorganic units to follow the crystal 2_1-
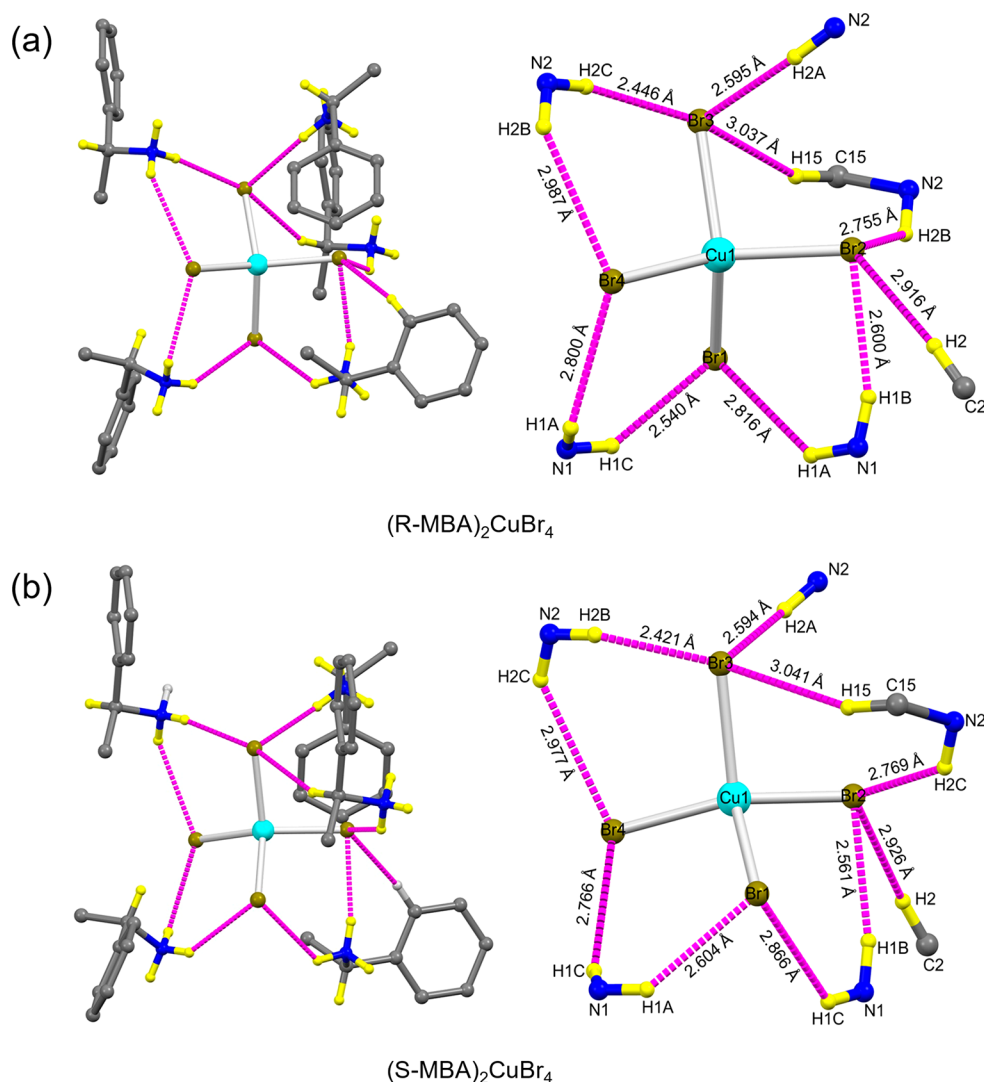
Figure 2. Hydrogen bonding network (N−H···Br and C−H···Br) connect the organic spacer (R-/S-MBA) with the inorganic CuBr$_4$ tetrahedral unit. The magenta dotted line represents H-bonding between Br and H. (a, b) Left: all the possible H-bonding interactions within the van der Waals limit of (H···Br) for the R- and S-chiral configured MBA$_2$CuBr$_4$ samples, respectively. Right: the H-bonding distances are mentioned. Other atoms are omitted for clarity. Cyan, olive, blue, yellow, and gray color denotes the Cu, Br, N, H, and C atoms, respectively.

screw axis. While this quasi-0D structure of CuBr$_4$ units makes it possible for the inorganic units to structurally follow the chirality dictated by the chiral organic components more effectively than in the case of the more rigid corner-shared 2D PbX$_6$ (X = I, Br, or Cl) units in the lead halide case, structural data together with theoretical analyses suggest an interesting connectivity between the otherwise isolated 0D CuBr$_4$ tetrahedral units established via a range of Cu−Br···Br−Cu halide pathways. This imparts a weak 2D character to the network of CuBr$_4$ units within the inorganic layer that is crucial for broadband chirality-dependent absorption properties.

The crystal structures of (R-/S-MBA)$_2$CuBr$_4$ (Figure 1a) have a central Cu atom coordinated by four Br atoms, forming [CuBr$_4$]$^{2-}$ tetrahedral units that are sandwiched between two layers of chiral R-/S-MBA spacer molecules. Both (R-/S-MBA)$_2$CuBr$_4$ crystallize in the orthorhombic crystal system having a nonpolar but chiral space group $P2_12_12_1$ with $Z = 4$ (crystallographic details are given in the Table S1). The asymmetric unit in both structures contains two R-/S-MBA cations and one CuBr$_4$ tetrahedral unit where all atoms are in

general crystallographic Wyckoff position "4a" of the space group $P2_12_12_1$. The CuBr$_4$ tetrahedral units in both crystals are highly distorted and away from regular geometry of 109.47° with Br−Cu−Br angles ranging from ∼97° to 134° (Figure S1 and Table S2). Hence, we used the bond angle variance equation $\sigma_{tet}^2 = \frac{1}{5} \sum_i [\alpha_i - 109.47]^2$ (where α_i are individual Br−Cu−Br bond angles) to quantify the amount of distortion in both the tetrahedral units.[25] The calculated σ_{tet}^2 values of 269.3 and 268.9 for R and S configurations, respectively, confirm the high distortion for the CuBr$_4$ tetrahedral units. This could be due to the high Jahn−Teller distortion for Cu^{2+} ions. Unlike in the cases of lead halides with corner-sharing PbX$_6$ (X = I, Br, or Cl) units leading to a 2D layered structure, the connectivities between otherwise isolated CuBr$_4$ tetrahedral units are established via short (3.86 Å) halide pathways (Cu−Br···Br−Cu), further strengthened by longer (4.43 Å) halide connectivities, giving rise to a 1D zigzag network of CuBr$_4$ units along the a axis, as shown in Figure 1c. These zigzag 1D networks of CuBr$_4$ are in turn, connected along the b
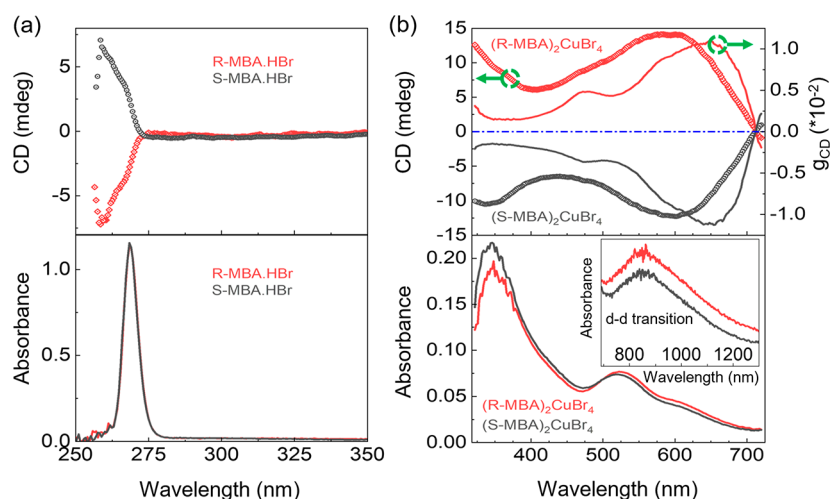
Figure 3. (a) CD (top panel) and absorption (bottom panel) spectra of chiral amine bromide salts dissolved in DMF (10 mg/mL). (b) CD (top panel, left axis) and absorption (bottom panel) spectra of the $(R\text{-/}S\text{-MBA})_2CuBr_4$ films. Top panel on the right axis describes the anisotropic factor g_{CD} of CD signal as a function of wavelength. Intraionic Cu d−d absorption in NIR region is shown in the inset of b, bottom panel.

axis by intermediate range (4.18 Å) halide interactions, establishing the weak 2D network of $CuBr_4$ units (see Figure 1c). Here the smallest Br⋯Br separation between adjacent tetrahedra is only 3.86 Å, approximately twice the ionic radius of the bromide ion (∼1.96 Å). The halide pathways (Cu−Br⋯Br−Cu) reported here (Figure 1c) for the compounds $(MBA)_2CuBr_4$ are significantly smaller than the other reported compounds (see Table S3) consisting of similar halide−halide (Cu−Br⋯Br−Cu) connectivity between otherwise isolated $[CuBr_4]^{2-}$ tetrahedral units. With the help of theoretical results, appearing in Figure S2, we have also shown that the Br⋯Br interactions in this structure lead to a substantial bandwidth of the Br p partial DOS with the extensive band dispersions along the inorganic layer directions, evidencing the weak 2D character. An extensive strong hydrogen bonding network (N−H⋯Br and C−H⋯Br) connects the organic spacer (R-/S-MBA) with the inorganic $[CuBr_4]^{2-}$ tetrahedra units (Figure 2 and Table S4). All hydrogen bonds present in both the crystals are within the van der Waals limit of (H⋯Br), i.e., 3.05 Å. The organic spacer transfers the chirality into the inorganic layer through these asymmetric hydrogen bonding, resulting in the symmetry related $CuBr_4$ tetrahedral units in the crystal to follow the 2_1-screw axis (Figure 1b). We note that the existence of individual $CuBr_4$ units without any corner sharing of common ligand ions in this quasi 0D structure, contrasting Pb-based 2D systems, makes it easier to transfer the chirality from the organic to the inorganic layer through hydrogen bonding. We have recorded the powder X-ray diffraction (PXRD) pattern of both samples (Figure S3a) which exactly matched the simulated PXRD patterns from single crystal structures, confirming the phase purity of the compounds. Additionally, we have carried out the profile fitting of PXRD patterns, which also confirm the same result (Figure S3b,c). Further, the X-ray diffraction patterns of film samples (Figure S3d) exhibit very narrow and sharp diffraction peaks, confirming the crystallinity of the as-prepared films, and display preferential orientation along the (00l) direction.

Figure 3a depicts the UV−vis absorption and CD spectra of the chiral amine bromide salts. Both R-MBA·HBr and S-MBA· HBr salts start to absorb in the UV region below ∼275 nm with a peak at ∼269 nm due to the $\pi \rightarrow \pi^*$ transition. Both R-

and S-chiral salts showed a mirrored CD below ∼275 nm, confirming their chirality. The absorption and CD spectra of the $(R\text{-/}S\text{-MBA})_2CuBr_4$ films are shown in Figure 3b. Both the films start to absorb at ∼710 nm and continue down to ∼470 nm. This broad absorption is due to partial 2D connectivity (Figure 1c) between individual $CuBr_4$ tetrahedral units, as ascertained by our theoretical results, discussed later in the text. The absorption in this entire region is due to the ligand-to-metal charge transfer (LMCT) transition, as previously reported for the tetrahedral $CuCl_4^{2-}$ species.[26,27] This absorption can be assigned to $Br\_p\sigma \rightarrow Cu\_d_{x^2-y^2}$ (centered at ∼525 nm) and $Br\_p\pi \rightarrow Cu\_d_{x^2-y^2}$ (centered at ∼607 nm) and, therefore, are associated with charge transfer (CT) states from ligand related orbitals to the antibonding half-filled Cu $d_{x^2-y^2}$ orbital. The absorption below ∼450 nm is related to the transitions from both occupied states of organic and inorganic to the unoccupied states of inorganic moieties. $(R\text{-/}S\text{-}$ $MBA)_2CuBr_4$ films showed a mirrored CD in the entire UV−vis region (∼710−325 nm), with the range being limited by the specific spectrometer used here. The chlorine analogue, $(R\text{-/}S\text{-MBA})_2CuCl_4$, in contrast, has CD limited[1,23] to below ∼490 nm due to a considerably larger bandgap than the Br compound here. A comparison of both the absorption and the CD spectra of chlorine[1,23] and bromine samples establishes a marked redshift of the band edge by ∼220 nm along with tuning the optical chirality over a larger wavelength region upon replacing the Cl with Br, in contrast to the results in ref 24. We show in Figure S4 a comparison of the absorption spectra of our sample and that of ref 24. along with the absorption spectrum of the Cl analogue, $(R\text{-MBA})_2CuCl_4$. While our result for the Br compound shows the expected red shift of the absorption edge with respect to the Cl sample, the absorption spectrum of the Br compound of ref 24. shows a blue shift. We note that our chiro-optical results in Figure 3b are also qualitatively different from those presented in ref 24, apparently for the same compound. These differences are illustrated in Figure S5 in terms of a direct comparison of our results with those obtained from results in ref 24.

The chiro-optical response is mainly governed by the nonzero electric and magnetic transition dipole moments in a

Table 1. Comparison of Chiral Anisotropy Factor (g_{CD}) of Chiral Hybrid Materials with Different Structural Dimensionality

Chemical formula	Dimensionality	g_{CD}	Peak wavelength (nm)	Absorption edge (nm)	Refs
(R-/S-MBA)$_2$SnI$_4$	2D	~1.3 × 10^{-3}	~450	~500	[16]
(R-/S-MBA)$_2$PbI$_4$	2D	~6 × 10^{-3}	~513	~520	[17]
(R-/S-MePEA)$_2$PbBr$_4$	2D	~10^{-4}	~400	~400	[30]
(R-/S-BPEA)$_2$PbI$_4$	2D	~3 × 10^{-3}	476	~552	[31]
(R-/S-β-MPA)$_2$MAPb$_2$I$_7$	2D bilayered	~2 × 10^{-3}	518	~575	[32]
(R-/S-NEA)$_2$PbI$_4$	2D	~3 × 10^{-3}	488	~500	[33]
R-/S-NEAPbI$_3$	1D	~0.04	395	~550	[33]
R-/S-PEAPbI$_3$	1D	~0.02	400	~425	[18]
(R-/S-1, 1-NEA)$_2$CuCl$_4$	0D	~0.01	~386 (within the LMCT band)	~450	[34]
(R-/S-1, 2-NEA)$_2$CuCl$_4$	0D	~2.9 × 10^{-3}	~386 (within the LMCT band)	~450	[34]
(R-MBA)$_2$CuCl$_4$	0D	~0.1	380 (within the LMCT band)	~490	[23]
(R-/S-MBA)$_2$CuBr$_4$	Partial 2D	0.011	~650 (within the LMCT band)	~710	This work

chiral space group, leading to a nonzero rotational strength (R) as

$$CD \propto R = Im[\langle \Psi_g | \hat{\mu} | \Psi_e \rangle \langle \Psi_e | \hat{m} | \Psi_g \rangle] = Im[\mu_{ge} m_{eg}] \quad (1)$$

where, Ψ_g and Ψ_e are the ground and excited state wave functions and μ_{ge} and m_{eg} are the electric and magnetic transition dipole moments, respectively. Since (R-/S-MBA)$_2$CuBr$_4$ crystallizes in a noncentrosymmetric chiral space group, $P2_12_12_1$, both μ_{ge} and m_{eg} are finite, making the compounds CD active. The anisotropy factor, g_{CD} is calculated as[28]

$$g_{CD} = \frac{CD[mdeg]}{32980 \times A} \quad (2)$$

where A is the conventional absorbance of nonpolarized light and CD is the differential absorbance of left and right circularly polarized lights, respectively. The anisotropy g_{CD} factor is independent of concentration and path length, since both absorbance and CD measurements are performed on the same sample. CD signals of these samples have the highest g_{CD} value of 0.011 (Figure 3b, top panel right axis) at the LMCT band (~650 nm). We note that this is the highest value of g_{CD} in the orange-red part of the visible spectrum reported for any hybrid material so far.

We compare all reported g_{CD} values of hybrid compounds in terms of their maximum values in Table 1 along with the wavelength at which this maximum appears; we have also indicate the dimensionality of the structure involved and the absorption edge in each case. In collecting these data, we have uniformly referred to the maximum g_{CD} observed within the LMCT band of the Cu halide systems, as it pertains to the electronic structure of the inorganic part; there are often chiro-optical activities in such systems at much shorter wavelengths arising purely from the participation of the chiral organic molecules. In all cases, we find that the absorption edge is at a shorter wavelength than ~650 nm, where our sample exhibits the highest g_{CD} value. The comparison of the g_{CD} values between different compounds in Table 1 reveals some interesting trends. For example, we did not find any example of a chiral system with a 3D structure. Moreover, the 2D chiral systems appear to have the maximum g_{CD} in the range of ~10^{-3}, in contrast to lower dimensional 1D and 0D structures that exhibit g_{CD} typically an order of magnitude higher. An order of magnitude change in the g_{CD} value with a change in dimensionality can be attributed to the structural rigidity within the inorganic layer. While the 1D and 0D structures of inorganic units make it possible for the inorganic units to

structurally follow the chirality dictated by the chiral organic components more effectively than in the case of the more rigid corner-shared 2D BX$_6$ (B = Pb and Sn; X = I and Br) units in the lead/tin halide case. The relationship between the structure and the chiro-optical activity of chiral hybrid lead halide materials has also been discussed based on 2D and 1D systems in ref 29.

It is interesting at this stage to contrast the structure and properties[1,23] of the chloride analogue (MBA)$_2$CuCl$_4$ with the present bromide compound since the chloride compound exhibits an order of magnitude higher g_{CD} value (see Table 1). (MBA)$_2$CuCl$_4$ crystallizes in a monoclinic crystal system with a chiral and polar space group C2 with Z = 2. The CuCl$_4$ tetrahedral units in both R and S configured compounds are considerably more distorted compared to its bromide analogue and deviate from regular tetrahedron of 109.47° with Cl−Cu−Cl angles ranging from ~91.5° to 96° (Figure S6 and Table S5), thus [CuCl$_4$]$^{2-}$ complex ions are closer to the square planar geometry. Significantly for the chloride analogue, the halide pathways (Cu−Cl⋯Cl−Cu) distances are 4.26 and 4.30 Å along the a and b axis, respectively (see Figure S7), much longer than the double of the ionic radius of chloride ion (1.81 Å), essentially forming isolated CuCl$_4$ tetrahedral units in 0D arrangements, unlike the weakly 2D nature of the Br compound presented here. This makes it a lot easier to drive the isolated CuCl$_4$ units to adopt the screw axis, making its electronic structure prominently chiral. The Br⋯Br con-nectivity, imparting the weak 2D nature in the bromide compound, makes it somewhat more difficult to make the inorganic units chiral, but not as difficult as in the case of truly 2D structures found for the Pb and Sn based compounds. In addition, the Br⋯Br interactions also help achieve the large Br derived bandwidths, as shown later in the text with the help of theoretical calculations, thereby extending the chiral activities to a considerably longer wavelength. In this sense, the Br compound presents a unique compromise of a partial 2D character of the inorganic layer that allows for the chirality driven from the organic to the inorganic while also at the same time allowing for a broadband chiro-optical activity extending to long wavelengths.

A comparison of the results in Figures 3a and b clearly establishes that the incorporation of R- and S-configured chiral organic cations induces optical chirality in a wavelength range that is way beyond those of the chiral molecules themselves and into the range contributed by the inorganic components of the 2D layered compound. The asymmetric H-bonding between the NH$_3^+$ group of the chiral amine and Br$^-$ of the
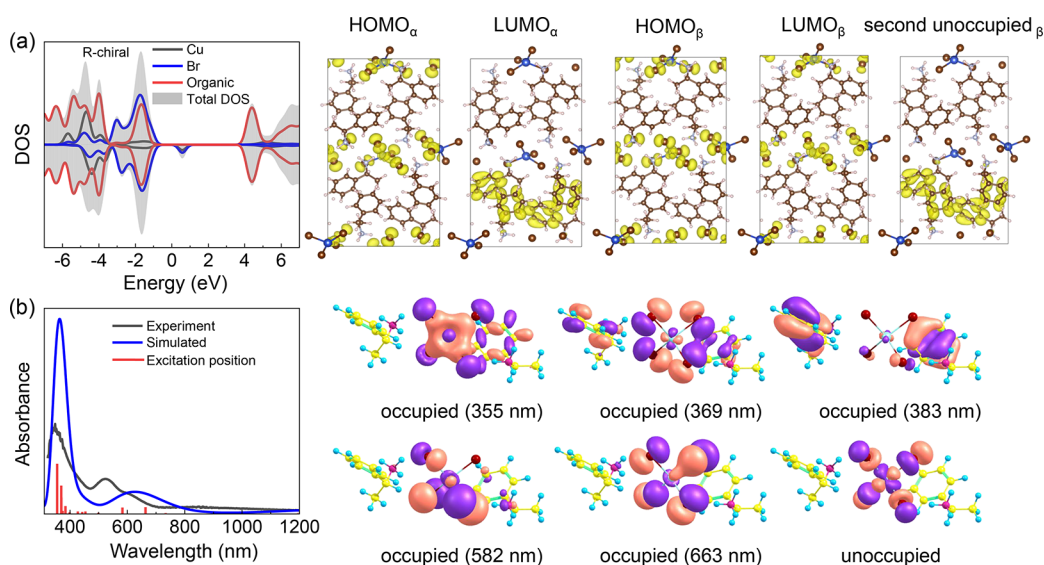
Figure 4. (a) Left: Projected density of states (black, blue, and red lines represent Cu, Br, and organic states, shaded region represents total DOS) and right: isodensity plots of the band edge wave functions for the (R-MBA)$_2$CuBr$_4$ compound. The calculated Fermi energy (0.7676 eV) has been set to zero in the DOS plot. (b) Left: TDDFT-simulated absorption spectrum of isolated single formula unit of (R-MBA)$_2$CuBr$_4$ compared to the experimental spectrum. Right: occupied and unoccupied orbitals involved in the major absorption peaks (355, 369, 383, 582, and 663 nm). The occupied orbitals with highest coefficient for each transition has been shown. The full list of all the possible orbitals involved and their corresponding coefficient are provided in the Supporting Information (Figure S8 and Text S1).

[CuBr$_4$]$^{2-}$ tetrahedra makes the inorganic layer itself chiral, and this is responsible for the chirality transfer from the organic component to the inorganic layer, resulting in the chiro-optical property of the 2D layered compound over a wide range of wavelengths. An additional contribution to the absorption spectra of (R-/S-MBA)$_2$CuBr$_4$ is present below the bandgap with weaker and broad features ranging from 730 to 1200 nm (see inset of Figure 3b bottom panel). This absorption band can be assigned to d−d transitions within the d orbitals of Cu.[26] Unfortunately, our experimental facilities cannot measure the CD beyond 725 nm, although we expect these d-d transitions also to be chirally active.

To gain insight into the electronic structure of the (R-/S-MBA)$_2$CuBr$_4$ compound, Density Functional Theory (DFT) calculations were carried out for both the R- and S-configurations. As expected, the two enantiomers show the same electronic and linear optical properties; here we present results from calculations on the R-compound. Figure 4a shows the spin-polarized site-projected partial densities of states (DOS) with the contributions of different atomic species with α and β denoting the up- and down-spin channels. It is evident in this figure that there is a substantial (∼2.6 eV) bandwidth associated with the leading occupied states that are dominated by Br contributions. This is a reflection of the Cu−Br···Br−Cu connectivity highlighted in Figure 1c, imparting this otherwise 0D system a partial 2D character. This is critically important to reduce the bandgap in this material and also to give rise to a broadband absorption and chiro-optical properties. Furthermore, we see that the leading states of Br are also strongly admixed with electronic states coming from the organic unit in the energy interval between −1 and −2.4 eV. This strong electronic coupling between the organic and the inorganic units is crucial to drive the rotation of the CuBr$_4$ along the 2$_1$ screw axis transferring the chirality of the organic molecule to the inorganic subunits. The calculated HOMO$_\beta$−LUMO$_\beta$ band gap is 1.45 eV. As we can see from the DOS and the band edge wave functions in Figure 4a, the main contribution

to the occupied band is associated with the Br and organic cation species coupled with a small Cu contribution, whereas the first unoccupied band in the down channel is mainly associated with Cu and Br contributions. Thus, the band edge contributions establish the fundamental bandgap excitation to be an LMCT transition from Br to Cu, observable in the experimental absorbance spectra between 470 to 710 nm. To accurately quantify the transition, we simulated the absorbance spectra, as shown in Figure 4b, for the isolated single formula unit of (R-MBA)$_2$CuBr$_4$, truncated from the periodic structure. It is noteworthy to mention that the CuBr$_4$ units of the periodic structure are only weakly connected with each other; thus, the consideration of the one isolated unit is adequate to mimic the periodic structure for calculating the absorbance spectra. Figure 4b shows that the simulated spectrum nicely matches that from the experiment. While identifying the orbitals involved with the major transitions in the <500 and 500−800 nm regions, we find that the two major transitions between 500 and 800 nm are at 582 and 663 nm, corresponding to the transition from Br p to the antibonding orbital comprised of a combination of Cu d$_{x^2-y^2}$ and Br p orbitals (see Figure 4b). On the other hand, the major peaks below 500 nm are found at 355, 369, and 383 nm, corresponding to the transitions from the orbitals of organic σ/π, bonding orbital composed of Cu d$_{xz}$/d$_{yz}$/d$_{xy}$/d$_{z^2}$ and Br p to the antibonding orbital composed of the combination of Cu d$_{x^2-y^2}$ and Br p orbitals (see right panels in Figure 4b). Therefore, it is clear from our analysis that the <500 nm transitions are not fully governed by the organic moiety; rather these transitions are to be understood as arising from both organic and inorganic moieties to the antibonding levels of the inorganic moiety, thus giving an indication of the transfer of the chirality from the organic to inorganic moiety.

In summary, we have synthesized both single crystals and films of partial 2D (R-/S-MBA)$_2$CuBr$_4$, exhibiting extensive chirality over almost the entire visible range. They show the highest values of g_{CD}, the concentration- and path length-

independent chiral anisotropy factor, in the orange-red part of the visible spectrum among all hybrid materials so far reported. Our results show that the chirality transfers from organic molecules to inorganic layers through an extensive asymmetric hydrogen bonding network and electronic coupling between the Br states and the electronic states in the organic unit, forcing the $CuBr_4$ tetrahedral units to follow the 2_1-screw axis. At the same time, the use of Br leads to a reduction of the bandgap by a large amount ($\sim$0.8 eV) compared to the chlorine analogue, thereby extending the chiro-optical activities significantly to longer wavelengths. The interesting structural aspect of this compound that underlies its interesting broadband chiro-optical properties extending to longer wavelengths is that it behaves as a quasi 0D system of $CuBr_4$ units allowing for the chirality transfer from the organic to the inorganic, while the weak 2D character arising from Cu—Br⋯Br—Cu interactions gives rise to the lowering of the bandgap and a broadband optical activity.

■ EXPERIMENTAL SECTION

Synthesis of R-MBA·HBr and S-MBA·HBr single crystals: R-MBA·HBr was synthesized by reacting R-MBA and 48% aqueous HBr with a molar ratio of 1:1.4. The hydrobromic acid was added dropwise into the R-MBA in a round-bottom flask in an ice bath with constant stirring. After $\sim$1.5 h of stirring, the resulting solution was evaporated with the rotary evaporator to get the crystals of R-MBA·HBr. This solid was washed thoroughly with diethyl ether and then recrystallized with anhydrous ethanol. Finally, the crystals were collected by filtration and stored under a vacuum for 24 h. The same procedure was followed with S-MBA to synthesize S-MBA·HBr.

Synthesis of $(R-MBA)_2CuBr_4$ and $(S-MBA)_2CuBr_4$ films: Glass substrates (1.5×1.5 cm^2) were washed sequentially with soap water, deionized water, acetone, and ethanol in an ultrasonic bath for 15 min each. Then, the substrates were further cleaned with UV-ozone treatment to improve the wettability. $CuBr_2$ and recrystallized chiral amine salt with a 1:2 molar ratio were dissolved in 0.5 mL of N,N-dimethylformamide (DMF) with a specific concentration (0.5 M) as the precursor solution. The thin films were fabricated with the precursor solution by a spin-coating method at 2000 rpm for 30 s, followed by annealing at 90 °C for 2 h on a hot plate to induce crystallization. Finally, the films were stored under vacuum for 48 h, which allows the complete crystallization, and then used for the measurements.

Synthesis of $(R-MBA)_2CuBr_4$ and $(S-MBA)_2CuBr_4$ single crystals: 1:2 molar ratio of $CuBr_2$ and recrystallized chiral amine salts were dissolved in 2 mL of aqueous (48%) HBr. The resulting solutions were heated at 60 °C for 2 h with constant stirring. After complete evaporation of the solvent, the micrometer-sized crystals formed; finally, these crystals were washed with diethyl ether and stored under reduced pressure.

Characterization and optical properties: The phase purities of powder and film samples were confirmed by X-ray diffraction (XRD) pattern collected with a Panalytical Philips diffractometer with Cu-K_α as the radiation source. Single-crystal X-ray diffraction data were collected on a Bruker Apex II diffractometer equipped with a CCD detector and using a monochromatic Mo Kα (λ = 0.71073 Å) X-radiation source. The voltage and current setting of the X-ray generator was kept at 50 kV and 30 mA, respectively. The data collection, reduction, and integration were performed using APEX3

software of Bruker. The structure solution and refinement were carried out using SHELXS and SHELXL included in the WinGX suite.[35−37] UV−visible absorption spectra were collected in the transmission mode on films using a UV−vis-NIR spectrometer (PerkinElmer lambda 750 UV−vis spectrometer with an integrating sphere). Circular dichroism (CD) measurements on both films and solutions were carried out in a J-715 (from JASCO) spectropolarimeter instrument.

■ COMPUTATIONAL DETAILS

First-principles calculations based on density functional theory (DFT) were carried out as implemented in the PWSCF Quantum-Espresso package.[38] Geometry optimization is performed using the GGA-PBE[39] level of theory, and the electron−ion interactions were described by the ultrasoft pseudopotentials with electrons from Br 4s, 4p; N, C 2s, 2p; H 1s; Cu 3s, 3p, 3d, 4s shells explicitly included in calculations, using a cutoff on the wave functions of 25 Ryd (200 Ryd on the charge density). Electronic structure calculations were performed by single-point spin-polarized hybrid calculations using the HSE06 functional[40] including 25% Hartree−Fock exchange with scalar-relativistic norm-conserving pseudo potentials with electrons from Br 4s, 4p; N, C 2s, 2p; H 1s; Cu 3s, 3p, 3d, 4s shells explicitly included in the calculations, using a cutoff on the wave functions of 40 Ryd (80 Ryd on the charge density). The experimental cell parameters were used in all the cases. A k-point sampling[41] of $4 \times 2 \times 1$ was used for both geometry optimizations and electronic structure calculations. For the TD-DFT calculations, an unrestricted B3LYP exchange-correlation functional has been used with 6-311G* basis sets using the Gaussian 09 software package.[42]

■ ASSOCIATED CONTENT

Ⓢⓘ Supporting Information

The Supporting Information is available free of charge at https://pubs.acs.org/doi/10.1021/acsmaterialslett.3c00268.

> Crystallographic details, bond angles, H bond distances, X-ray diffraction patterns, orbitals with coefficients, and orbitals involved in various transitions, electronic structure (PDF)

Accession Codes

CCDC 2201343 and 2201433 contain the supplementary crystallographic data for this paper. These data can be obtained free of charge via www.ccdc.cam.ac.uk/data_request/cif, or by emailing data_request@ccdc.cam.ac.uk, or by contacting The Cambridge Crystallographic Data Centre, 12 Union Road, Cambridge CB2 1EZ, UK; fax: +44 1223 336033.

■ AUTHOR INFORMATION

Corresponding Author

D. D. Sarma − *Solid State and Structural Chemistry Unit, Indian Institute of Science, Bengaluru 560012, India;* ⓞ orcid.org/0000-0001-6433-1069; Email: sarma@iisc.ac.in

Authors

Ranjan Das − *Solid State and Structural Chemistry Unit, Indian Institute of Science, Bengaluru 560012, India;* ⓞ orcid.org/0000-0002-0029-0170

Modasser Hossain − *Centre for Nano and Soft Matter Sciences (CeNS), Bengaluru 562162, India; Manipal*

Academy of Higher Education (MAHE), Manipal 576104, India; orcid.org/0000-0003-1437-8162

Arup Mahata − *Computational Laboratory for Hybrid/ Organic Photovoltaics (CLHYO), Istituto CNR di Scienze e Tecnologie Chimiche "Giulio Natta" (CNR-SCITEC), Perugia 06123, Italy; Department of Chemistry, Indian Institute of Technology Hyderabad, Kandi, Sangareddy, Telangana 502285, India;* orcid.org/0000-0002-4995-3326

Diptikanta Swain − *Institute of Chemical Technology-IndianOil Odisha Campus, Bhubaneswar 751013, India;* orcid.org/0000-0003-4048-5017

Filippo De Angelis − *Computational Laboratory for Hybrid/ Organic Photovoltaics (CLHYO), Istituto CNR di Scienze e Tecnologie Chimiche "Giulio Natta" (CNR-SCITEC), Perugia 06123, Italy; Department of Chemistry, Biology and Biotechnology, University of Perugia, Perugia 06123, Italy; Department of Natural Sciences & Mathematics, College of Sciences & Human Studies, Prince Mohammad Bin Fahd University, Al Khobar 31952, Kingdom of Saudi Arabia;* orcid.org/0000-0003-3833-1975

Pralay K. Santra − *Centre for Nano and Soft Matter Sciences (CeNS), Bengaluru 562162, India;* orcid.org/0000-0002-1951-5835

Complete contact information is available at:
https://pubs.acs.org/10.1021/acsmaterialslett.3c00268

Notes
The authors declare no competing financial interest.

REFERENCES

(1) Guo, Z.; Li, J.; Wang, C.; Liu, R.; Liang, J.; Gao, Y.; Cheng, J.; Zhang, W.; Zhu, X.; Pan, R.; He, T. Giant Optical Activity and Second Harmonic Generation in 2D Hybrid Copper Halides. *Angew. Chem., Int. Ed.* **2021**, *60*, 8441−8445.

(2) Ma, J.; Fang, C.; Chen, C.; Jin, L.; Wang, J.; Wang, S.; Tang, J.; Li, D. Chiral 2D Perovskites with a High Degree of Circularly Polarized Photoluminescence. *ACS Nano* **2019**, *13*, 3659−3665.

(3) Taniguchi, K.; Nishio, M.; Abe, N.; Huang, P.-J.; Kimura, S.; Arima, T.-h.; Miyasaka, H. Magneto-Electric Directional Anisotropy in Polar Soft Ferromagnets of Two-Dimensional Organic−Inorganic Hybrid Perovskites. *Angew. Chem., Int. Ed.* **2021**, *60*, 14350−14354.

(4) Huang, P. J.; Taniguchi, K.; Miyasaka, H. Bulk Photovoltaic Effect in a Pair of Chiral-Polar Layered Perovskite-Type Lead Iodides Altered by Chirality of Organic Cations. *J. Am. Chem. Soc.* **2019**, *141*, 14520−14523.

(5) Wang, Y.; Xu, J.; Wang, Y.; Chen, H. Emerging Chirality in Nanoscience. *Chem. Soc. Rev.* **2013**, *42*, 2930−2962.

(6) Li, S.; Veksler, M.; Xu, Z.; Xu, L.; Xu, C.; Kotov, N. A. Self-Assembly of Earth-Abundant Supraparticles with Chiral Interstices for Enantioselective Photocatalysis. *ACS Energy Lett.* **2021**, *6*, 1405−1412.

(7) Di Bari, L.; Pescitelli, G.; Salvadori, P. Conformational Study of 2,2′-Homosubstituted 1,1′-Binaphthyls by Means of UV and CD Spectroscopy. *J. Am. Chem. Soc.* **1999**, *121*, 7998−8004.

(8) Kulkarni, S. A.; Baikie, T.; Boix, P. P.; Yantara, N.; Mathews, N.; Mhaisalkar, S. Band-Gap Tuning of Lead Halide Perovskites Using a Sequential Deposition Process. *J. Mater. Chem. A* **2014**, *2*, 9221−9225.

(9) Hao, F.; Stoumpos, C. C.; Chang, R. P. H.; Kanatzidis, M. G. Anomalous Band Gap Behavior in Mixed Sn and Pb Perovskites Enables Broadening of Absorption Spectrum in Solar Cells. *J. Am. Chem. Soc.* **2014**, *136*, 8094−8099.

(10) Galkowski, K.; Surrente, A.; Baranowski, M.; Zhao, B.; Yang, Z.; Sadhanala, A.; Mackowski, S.; Stranks, S. D.; Plochocka, P. Excitonic Properties of Low-Band-Gap Lead-Tin Halide Perovskites. *ACS Energy Lett.* **2019**, *4*, 615−621.

(11) Galkowski, K.; Mitioglu, A.; Miyata, A.; Plochocka, P.; Portugall, O.; Eperon, G. E.; Wang, J. T.-W.; Stergiopoulos, T.; Stranks, S. D.; Snaith, H. J.; Nicholas, R. J. Determination of the Exciton Binding Energy and Effective Masses for Methylammonium and Formamidinium Lead Tri-Halide Perovskite Semiconductors. *Energy Environ. Sci.* **2016**, *9*, 962−970.

(12) Zhumekenov, A. A.; Saidaminov, M. I.; Haque, M. A.; Alarousu, E.; Sarmah, S. P.; Murali, B.; Dursun, I.; Miao, X. H.; Abdelhady, A. L.; Wu, T.; Mohammed, O. F.; Bakr, O. M. Formamidinium Lead Halide Perovskite Crystals with Unprecedented Long Carrier Dynamics and Diffusion Length. *ACS Energy Lett.* **2016**, *1*, 32−37.

(13) Dong, Q.; Fang, Y.; Shao, Y.; Mulligan, P.; Qiu, J.; Cao, L.; Huang, J. Electron-Hole Diffusion Lengths > 175 μm in Solution-Grown CH3NH3PbI3 Single Crystals. *Science* **2015**, *347*, 967−970.

(14) Herz, L. M. Charge-Carrier Mobilities in Metal Halide Perovskites: Fundamental Mechanisms and Limits. *ACS Energy Lett.* **2017**, *2*, 1539−1548.

(15) Ahn, J.; Lee, E.; Tan, J.; Yang, W.; Kim, B.; Moon, J. A New Class of Chiral Semiconductors: Chiral-Organic-Molecule-Incorporating Organic−Inorganic Hybrid Perovskites. *Mater. Horiz.* **2017**, *4*, 851−856.

(16) Lu, H.; Xiao, C.; Song, R.; Li, T.; Maughan, A. E.; Levin, A.; Brunecky, R.; Berry, J. J.; Mitzi, D. B.; Blum, V.; Beard, M. C. Highly Distorted Chiral Two-Dimensional Tin Iodide Perovskites for Spin Polarized Charge Transport. *J. Am. Chem. Soc.* **2020**, *142*, 13030−13040.

(17) Ahn, J.; Ma, S.; Kim, J.-Y.; Kyhm, J.; Yang, W.; Lim, J. A.; Kotov, N. A.; Moon, J. Chiral 2D Organic Inorganic Hybrid Perovskite with Circular Dichroism Tunable Over Wide Wavelength Range. *J. Am. Chem. Soc.* **2020**, *142*, 4206−4212.

(18) Chen, C.; Gao, L.; Gao, W.; Ge, C.; Du, X.; Li, Z.; Yang, Y.; Niu, G.; Tang, J. Circularly Polarized Light Detection Using Chiral Hybrid Perovskite. *Nat. Commun.* **2019**, *10*, 1927.

(19) Ma, S.; Ahn, J.; Moon, J. Chiral Perovskites for Next-Generation Photonics: From Chirality Transfer to Chiroptical Activity. *Adv. Mater.* **2021**, *33*, 2005760.

(20) Dang, Y.; Liu, X.; Sun, Y.; Song, J.; Hu, W.; Tao, X. Bulk Chiral Halide Perovskite Single Crystals for Active Circular Dichroism and Circularly Polarized Luminescence. *J. Phys. Chem. Lett.* **2020**, *11*, 1689−1696.

(21) Ma, J.; Wang, H.; Li, D. Recent Progress of Chiral Perovskites: Materials, Synthesis, and Properties. *Adv. Mater.* **2021**, *33*, 2008785.

(22) Jana, M. K.; Song, R.; Liu, H.; Khanal, D. R.; Janke, S. M.; Zhao, R.; Liu, C.; Valy Vardeny, Z.; Blum, V.; Mitzi, D. B. Organic-to-

Inorganic Structural Chirality Transfer in a 2D Hybrid Perovskite and Impact on Rashba-Dresselhaus Spin-Orbit Coupling. *Nat. Commun.* **2020**, *11*, 1−10.

(23) Hao, J.; Lu, H.; Mao, L.; Chen, X.; Beard, M. C.; Blackburn, J. L. Direct Detection of Circularly Polarized Light Using Chiral Copper Chloride-Carbon Nanotube Heterostructures. *ACS Nano* **2021**, *15*, 7608−7617.

(24) Lu, Y.; Wang, Q.; He, R.; Zhou, F.; Yang, X.; Wang, D.; Cao, H.; He, W.; Pan, F.; Yang, Z.; Song, C. Highly Efficient Spin-Filtering Transport in Chiral Hybrid Copper Halides. *Angew. Chem., Int. Ed.* **2021**, *60*, 23578−23583.

(25) Robinson, K.; Gibbs, G. V.; Ribbe, P. H. Quadratic Elongation: A Quantitative Measure of Distortion in Coordination Polyhedra. *Science* **1971**, *172*, 567−570.

(26) Willett, R. D.; Liles, O. L.; Michelson, C. Electronic Absorption Spectra of Monomeric Copper(II) Chloride Species and the Electron Spin Resonance Spectrum of the Square-Planar CuCl42-Ion. *Inorg. Chem.* **1967**, *6*, 1885−1889.

(27) Cortecchia, D.; Dewi, H. A.; Yin, J.; Bruno, A.; Chen, S.; Baikie, T.; Boix, P. P.; Grätzel, M.; Mhaisalkar, S.; Soci, C.; Mathews, N. Lead-Free MA2CuClxBr4-x Hybrid Perovskites. *Inorg. Chem.* **2016**, *55*, 1044−1052.

(28) Wakabayashi, M.; Yokojima, S.; Fukaminato, T.; Shiino, K.; Irie, M.; Nakamura, S. Anisotropic Dissymmetry Factor, g: Theoretical Investigation on Single Molecule Chiroptical Spectroscopy. *J. Phys. Chem. A* **2014**, *118*, 5046−5057.

(29) Zhang, Z.; Wang, Z.; Sung, H. H. Y.; Williams, I. D.; Yu, Z. G.; Lu, H. Revealing the Intrinsic Chiroptical Activity in Chiral Metal-Halide Semiconductors. *J. Am. Chem. Soc.* **2022**, *144*, 22242−22250.

(30) Yan, L.; Jana, M. K.; Sercel, P. C.; Mitzi, D. B.; You, W. Alkyl-Aryl Cation Mixing in Chiral 2D Perovskites. *J. Am. Chem. Soc.* **2021**, *143*, 18114−18120.

(31) Peng, Y.; Liu, X.; Li, L.; Yao, Y.; Ye, H.; Shang, X.; Chen, X.; Luo, J. Realization of Vis-NIR Dual-Modal Circularly Polarized Light Detection in Chiral Perovskite Bulk Crystals. *J. Am. Chem. Soc.* **2021**, *143*, 14077−14082.

(32) Wang, L.; Xue, Y.; Cui, M.; Huang, Y.; Xu, H.; Qin, C.; Yang, J.; Dai, H.; Yuan, M. A Chiral Reduced-Dimension Perovskite for an Efficient Flexible Circularly Polarized Light Photodetector. *Angew. Chem., Int. Ed.* **2020**, *59*, 6442−6450.

(33) Ishii, A.; Miyasaka, T. Direct Detection of Circular Polarized Light in Helical 1D Perovskite-Based Photodiode. *Sci. Adv.* **2020**, *6*, 1−7.

(34) Guo, Z.; Li, J.; Liang, J.; Wang, C.; Zhu, X.; He, T. Regulating Optical Activity and Anisotropic Second-Harmonic Generation in Zero-Dimensional Hybrid Copper Halides. *Nano Lett.* **2022**, *22*, 846−852.

(35) Sheldrick, G. M. A Short History of SHELX. *Acta Cryst. A* **2008**, *64*, 112−122.

(36) Sheldrick, G. M. Crystal Structure Refinement with SHELXL. *Acta Cryst. C* **2015**, *71*, 3−8.

(37) Farrugia, L. J. WinGX Suite for Small-Molecule Single-Crystal Crystallography. *J. Appl. Crystallogr.* **1999**, *32*, 837−838.

(38) Giannozzi, P.; Baroni, S.; Bonini, N.; Calandra, M.; Car, R.; Cavazzoni, C.; Ceresoli, D.; Chiarotti, G. L.; Cococcioni, M.; Dabo, I.; et al. QUANTUM ESPRESSO: A Modular and Open-Source Software Project for Quantum Simulations of Materials. *J. Phys.: Condens. Matter* **2009**, *21*, 395502.

(39) Perdew, J. P.; Burke, K.; Ernzerhof, M. Generalized Gradient Approximation Made Simple. *Phys. Rev. Lett.* **1996**, *77*, 3865−3868.

(40) Heyd, J.; Scuseria, G. E.; Ernzerhof, M. Hybrid Functionals Based on a Screened Coulomb Potential. *J. Chem. Phys.* **2003**, *118*, 8207−8215.

(41) Monkhorst, H. J.; Pack, J. D. Special Points for Brillouin-Zone Integrations. *Phys. Rev. B* **1976**, *13*, 5188−5192.

(42) Frisch, M. J.; Trucks, G. W.; Schlegel, H. B.; Scuseria, G. E.; Robb, M. a.; Cheeseman, J. R.; Scalmani, G.; Barone, V.; Petersson, G. a.; Nakatsuji, H.; Li, X.; Caricato, M.; Marenich, a. V.; Bloino, J.; Janesko, B. G.; Gomperts, R.; Mennucci, B.; Hratchian, H. P.; Ortiz, J. V.; Izmaylov, a. F.; et al. *Gaussian 16*, Revision C.01; Gaussian, Inc.: Wallingford, CT.